Cell Reports
Methods

Article

Label-free imaging of 3D pluripotent stem cell differentiation dynamics on chip

Graphical abstract

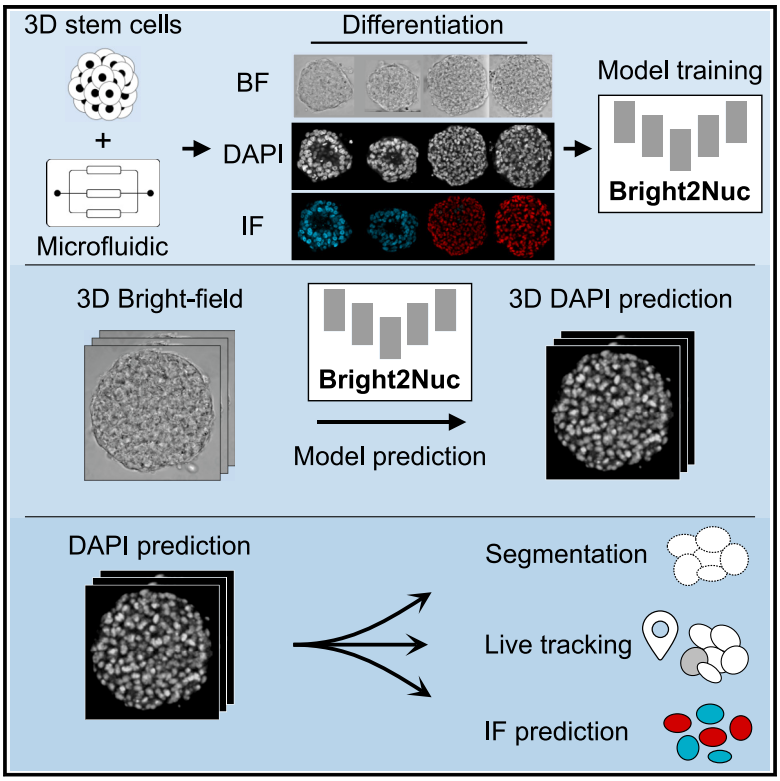

Highlights

- Large-scale integration of 3D stem cell cultures on a microfluidic chip
- An AI imaging tool is developed to predict nuclei from bright-field image stacks
- Prediction of stem cell states from bright-field images along a time trajectory
- Tracking of single nuclei in 3D during stem cell differentiation

Authors

Scott Atwell, Dominik Jens Elias Waibel, Sayedali Shetab Boushehri, Sandra Wiedenmann, Carsten Marr, Matthias Meier

Correspondence

carsten.marr@helmholtz-munich.de (C.M.), matthias.meier@helmholtz-munich.de (M.M.)

In brief

Atwell et al. develop an AI imaging tool to predict nuclei within 3D stem cell cultures from bright-field images. Combining the AI imaging strategy with a microfluidic large-scale integration cell culture chip platform, we are able to predict cell states, track single nuclei, or decrease image acquisition time for cell screening.

Atwell et al., 2023, Cell Reports Methods 3, 100523
July 24, 2023
https://doi.org/10.1016/j.crmeth.2023.100523

CellPress

Cell Reports Methods

CellPress
OPEN ACCESS

Article

Label-free imaging of 3D pluripotent stem cell differentiation dynamics on chip

Scott Atwell,[1,7] Dominik Jens Elias Waibel,[2,3,7] Sayedali Shetab Boushehri,[2,4,5] Sandra Wiedenmann,[1] Carsten Marr,[2,*] and Matthias Meier[1,6,8,*]

[1]Helmholtz Pioneer Campus, Helmholtz Zentrum München - German Research Center for Environmental Health, Neuherberg, Germany
[2]Institute of AI for Health, Helmholtz Zentrum München - German Research Center for Environmental Health, Neuherberg, Germany
[3]TUM School of Life Sciences, Technical University of Munich, Weihenstephan, Germany
[4]Department of Mathematics, Technical University of Munich, Munich, Germany
[5]Data & Analytics, Pharmaceutical Research and Early Development, Roche Innovation Center Munich (RICM), Penzberg, Germany
[6]Center for Biotechnology and Biomedicine, University of Leipzig, Leipzig, Germany
[7]These authors contributed equally
[8]Lead contact
*Correspondence: carsten.marr@helmholtz-munich.de (C.M.), matthias.meier@helmholtz-munich.de (M.M.)
https://doi.org/10.1016/j.crmeth.2023.100523

MOTIVATION Our work aims to meet the increasing demand for high-resolution single-cell phenotyping in 3D stem cell cultures. During the parallelization of 3D cell cultures, we faced the problem of acquiring high-resolution or high-time-resolved image data for phenotyping. However, single-cell resolution is required to characterize the heterogeneous cell populations as, for example, encountered within stem cell differentiation experiments. To address this challenge, we employed label-free imaging technology to stain nuclei *in situ* from 3D bright-field image sets, which reduces image acquisition time and enables the inference of cell types and velocity. The presented approach thus enables dynamic large-scale screening of 3D stem cell cultures based on bright-field imaging.

SUMMARY

Massive, parallelized 3D stem cell cultures for engineering *in vitro* human cell types require imaging methods with high time and spatial resolution to fully exploit technological advances in cell culture technologies. Here, we introduce a large-scale integrated microfluidic chip platform for automated 3D stem cell differentiation. To fully enable dynamic high-content imaging on the chip platform, we developed a label-free deep learning method called Bright2Nuc to predict *in silico* nuclear staining in 3D from confocal microscopy bright-field images. Bright2Nuc was trained and applied to hundreds of 3D human induced pluripotent stem cell cultures differentiating toward definitive endoderm on a microfluidic platform. Combined with existing image analysis tools, Bright2Nuc segmented individual nuclei from bright-field images, quantified their morphological properties, predicted stem cell differentiation state, and tracked the cells over time. Our methods are available in an open-source pipeline, enabling researchers to upscale image acquisition and phenotyping of 3D cell culture.

INTRODUCTION

New cell culture technologies for pluripotent stem cells are central to enabling *in vitro* disease models, regenerative therapies, and reducing animal studies for drug screens.[1] 3D culture techniques have become commonly used in differentiation trials of stem cells toward defined cell types, such as beta cells,[2] hepatocytes,[3] and intestinal epithelial cells.[4] Although 3D cultures can mimic the architecture of the tissue niche, promoting cell-to-cell and cell-to-matrix interactions, the chemical microenvironment requires additional technological tools. Microfluidic chip technologies can fill this gap by automating fluid programs to test complex differentiation protocols in parallelized stem cell cultures.[5] Further, microfluidics offers miniaturized solutions for unifying the shape and size of 3D stem cell cultures but also for positioning the cell cultures to simplify high-content data acquisition. With the progression of cell culture technologies, analytical methods to phenotype 3D cell cultures under higher-throughput conditions have become difficult because cells in 3D adopt high-density compact configurations, and cell morphologies are more heterogeneous and less recognizable than in 2D cultures. Thus, tracking and phenotyping massively

parallelized 3D cultures at the single-cell level presents the challenge of developing not only image acquisition methods that allow resolution of the 3D cell cultures in high time and spatial resolution but also powerful computational methods to handle the increasing amount of data being generated.[6]

Owing to the widely accessible equipment, confocal fluorescence is the gold standard for obtaining single-cell resolutions in optical microscopy. Real-time imaging of cell types, functions, or cell states is hampered by the need for fluorescent reporter cell lines, which often require lengthy processes to engineer and validate.[7] Furthermore, fluorescent reporters may affect biochemical phenomena or cell types of interest and induce cytotoxic stress under prolonged imaging times. Label-free microscopy, based on deep learning image processing and analysis, has emerged as an alternative to fluorescent reporters. For example, *in silico* staining can be used to predict fluorescent markers from the bright-field images of various tissue types.[8–11] Once trained, deep-learning models are fast and consistent in their predictions. For high-content imaging in screening studies, label-free microscopy can dramatically reduce the image acquisition time by inferring multiple fluorescent *in silico* stains from single images without being limited by spectral cross-talk. Most of the previous approaches have focused on high-resolution imaging of 2D cell cultures or tissue sections with high numerical apertures. Higher-throughput imaging results in a trade-off between acquisition time, resolution, and phototoxicity. In particular, a higher resolution is only achieved with liquid immersion objectives, which are cumbersome for high-content data acquisition. Further, though not unprecedented,[12] applications of *in silico* staining to live 3D cell cultures are rare. Finally, no previous approach has addressed the problem of phenotyping stem cells in a 3D environment from bright-field images.

Herein, we present a microfluidic platform for complex fluid programming in a multiplexed high-throughput manner to enable the differentiation of human induced pluripotent stem cells (hiPSCs) in 3D while simultaneously facilitating live imaging. We focused on acquiring imaging data on 3D cell cultures with a relatively low-resolution and low-numerical-aperture air-immersion 20× objective through confocal microscopy to increase data acquisition throughput. We introduced a deep learning-based method, named Bright2Nuc, to predict nuclear fluorescence within on-chip 3D cell cultures from low-magnification bright-field images. *In silico* staining images were used to infer the differentiation state of human stem cells and cell dynamics within on-chip cultivated 3D cell cultures undergoing endodermal differentiation. For reproducibility and applicability, the Bright2Nuc deep learning method and associated data were published using open-source software.

RESULTS

Imaging of 3D human stem cell cultures on chip

We developed a microfluidic large-scale integration chip platform[13] to automate the formation, culture, and differentiation of 128 3D cell cultures under 32 independent chemical conditions (Figure 1A). Cells were seeded as a single-cell suspension in each chamber (Video S1), and after 4 h, 3D cell cultures were formed by self-aggregation (Figure 1B). A chamber height of 50 μm constrained the 3D cell cultures between the glass substrate and PDMS channel top, ensuring imaging from top to bottom (Figure 1C). Together with the position stability of the cell culture compartments, the chip enabled high-content time-resolved imaging of reproducibly homogeneous (Figure S1A) live 3D cell cultures with temporal control of chemical conditions.

We applied our platform to definitive endoderm (DE) differentiation, a critical first step for differentiating liver, gut, pancreas, lungs, trachea, and thyroid cell types. hiPSC-derived 3D cultures could be differentiated on chip toward DE by activating the transforming growth factor β (TGF-β)/nodal and WNT signaling pathways with activin A and CHIR-99021, respectively. Over 3 days, the two chemical components were controlled in time and concentration using fluid programming. Upon fixation of subsets of 3D cell cultures with NHS-ester every 24 h, a differentiation trajectory was established. All cell cultures were immunostained on the chip at the end of differentiation for the pluripotency marker octamer-binding transcription factor 4 (OCT4) and the two DE-specific transcription factors (TFs) forkhead box A2 (FOXA2) and SRY-box 17 (SOX17). Bright-field and immunofluorescence (IF) images were recorded by standard confocal microscopy with an xy resolution of 0.25 μm/pixel (px) and a z resolution of 1 μm/plane. Quantitative fluorescence signals of the TFs were extracted per nucleus for all 3D cell cultures by segmenting the 3D DAPI signal using a retrained StarDist model.[14,15] All IF images were corrected for the signal decrease in the z direction caused by increasing light scattering and for the signal decrease in the xy direction caused by gradually decreasing penetration of labeled antibodies.

Within the first 24 h after the start of DE differentiation, 3D cell cultures lost an average of 42.6% ± 17.1% (mean ± SD, averaged over $N_r = 4$ biological replicates with a total of N = 426 cultures) of their surface area in the xy plane due to cell disaggregation (Figures S1B and S1D). After this initial cell loss, most of the cell cultures recovered and grew until the end of differentiation (Figure S1C). The individual growth behavior of 3D cell cultures varied depending on the initial cell loss, but TF expression during differentiation was comparable for all cell cultures, where hiPSCs lost the expression of the pluripotency marker OCT4 within the first 48 h and gained the expression of the DE-specific markers, FOXA2 and SOX17 (Figure 1D). Furthermore, on-chip differentiation resulted in a nearly homogeneous cell population with a yield as high as 96% ± 3% FOXA2/SOX17 double-expressing cells after 72 h (Figure 1E; mean ± SD, N = 14,936 nuclei in N = 20 cultures). However, experimental yields varied with an average of 90% ± 6% (mean ± SD, $N_r = 4$) of double-expressing cells at the end of differentiation, as previously observed in the standard cell well plate and chip culture formats.[16]

Label-free prediction of nuclei in 3D cell cultures

The full high-content imaging of hiSPC-derived 3D cell cultures with standard confocal microscopy with four fluorescence channels is laborious and time consuming, requiring approximately 48 h for IF staining and 48 h of imaging. To cope with the chip throughput and characterize live-cell cultures, we sought to predict the nuclear fluorescence of cells within whole 3D cell cultures along the DE differentiation trajectory from low-magnification bright-field images. For this purpose, we developed

CellPress
OPEN ACCESS

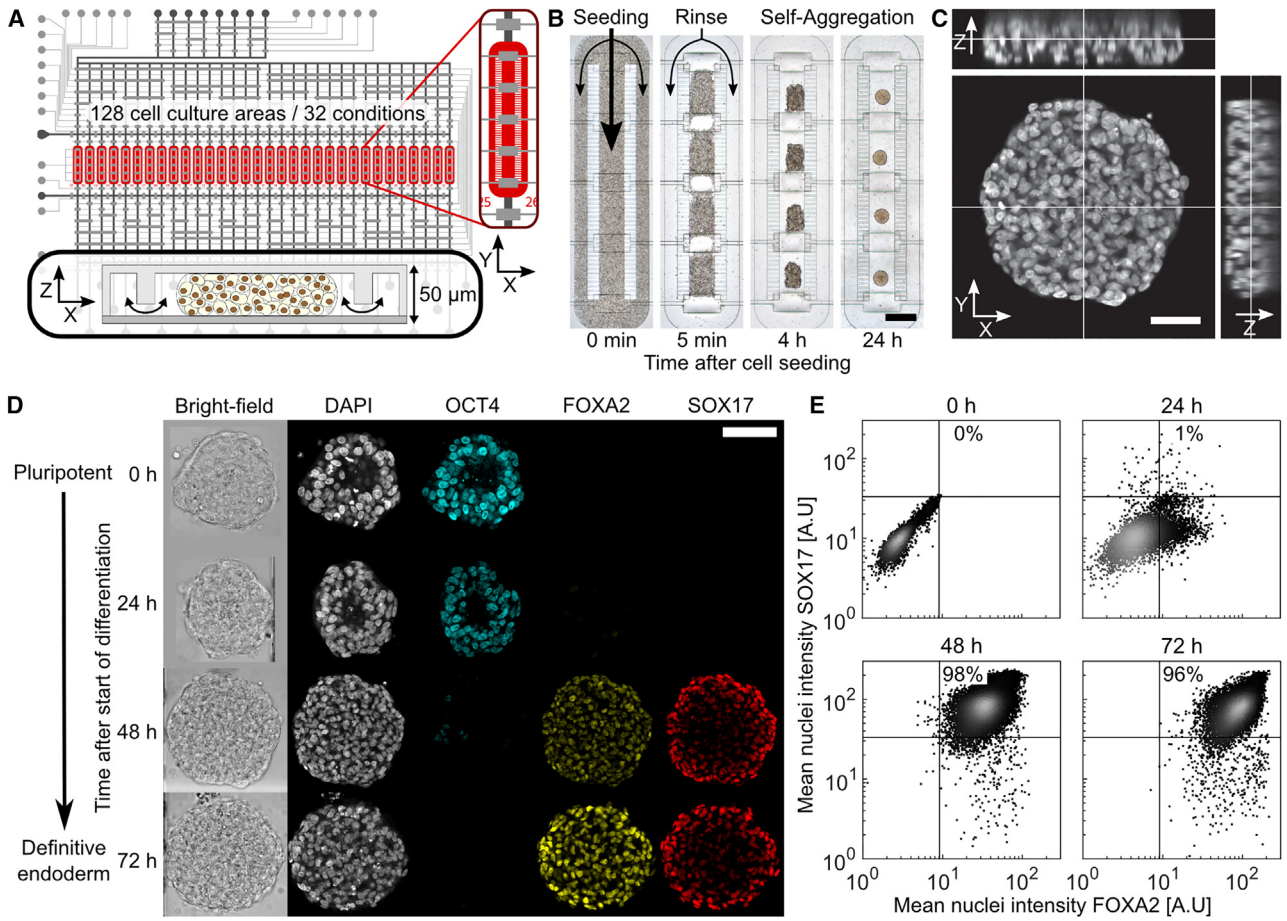

Figure 1. Microfluidic large-scale integration chip platform chip enables the multiplexed differentiation and imaging of 3D human induced pluripotent stem cell cultures

(A) Scheme of microfluidic large-scale integration chip layout. The black and gray lines denote the flow and control microchannels of the double-layered PDMS chip, respectively. The inset on the right shows a magnified view of one cell culture chamber (red). The bottom inset shows the cross-section through a filled cell culture area.

(B) On-chip 3D cell culture formation process: (1) seeding of single-cell solution, (2) separation of cell culture areas upon actuation of pneumatic membrane valves, followed by cell rinsing, and (3) self-aggregation of cells in the confined cell culture volume after 4 and 24 h. Scale bar: 500 µm.

(C) Orthogonal views of an on-chip 3D cell culture stained with DAPI. Images were taken with a 0.25 µm/px xy resolution and 1 µm/px z resolution. Scale bar: 50 µm.

(D) Immunofluorescence confocal images of 3D cell cultures fixed along the differentiation trajectory from the pluripotency (OCT4-positive) to the definitive endoderm (FOXA2 and SOX17 double-positive) cell stage. Scale bar: 100 µm.

(E) Quantitative image analysis of cell type marker expression along the differentiation trajectory within all cells of 3D cell cultures from a single chip run. Each data point represents the mean fluorescence intensity of individual nuclei segmented in 3D; the indicated percentages represent the fraction of FOXA2/SOX17 double-positive nuclei (nuclei considered: n_{0h} = 5,501, n_{24h} = 8,700, n_{48h} = 22,587, n_{72h} = 14,936) from multiple 3D cell cultures (N_{0h} = 12, N_{24h} = 25, N_{48h} = 24, N_{72h} = 30).

Bright2Nuc, a U-Net-based deep neural network (Figures 2A and 2B). Bright2Nuc incorporates the 3D information of bright-field images by taking three consecutive bright-field Z slices (Z = k, Z = k − 1, and Z = k + 1 positions) to compute the nucleus prediction of any given Z position (Z = k) (Figure 2B). The model was trained on 255 paired bright-field stacks and fluorescence nucleus images of 162 fixed and 93 live 3D cell cultures by minimizing the mean-squared pixel error between the paired predicted and true IF nucleus images (see experimental procedures). While images from fixed 3D cell cultures were acquired along the DE trajectory as described previously (Figure 1C), images from live 3D cell cultures were obtained in the pluripotent state using a SOX2-T2A-tdTomato fluorescence reporter hiPSC line (Video S2). To evaluate the performance of our Bright2Nuc model, we benchmarked the correlation between the pixel values of the ground-truth IF image and the *in silico* Bright2Nuc prediction at the 3D cell culture level (Figure 2F). We tested the model on an independent test set containing 85 cell cultures (N = 54 fixed and N = 31 live) from the same experiments used for training (in domain). We additionally evaluated Bright2Nuc's robustness on 123 cell cultures in a replicate experiment. The image data were excluded from the model training (out domain). Bright2Nuc results showed high correlations for in-domain (ρ = 0.79 ± 0.07, mean ± SD for N = 54)

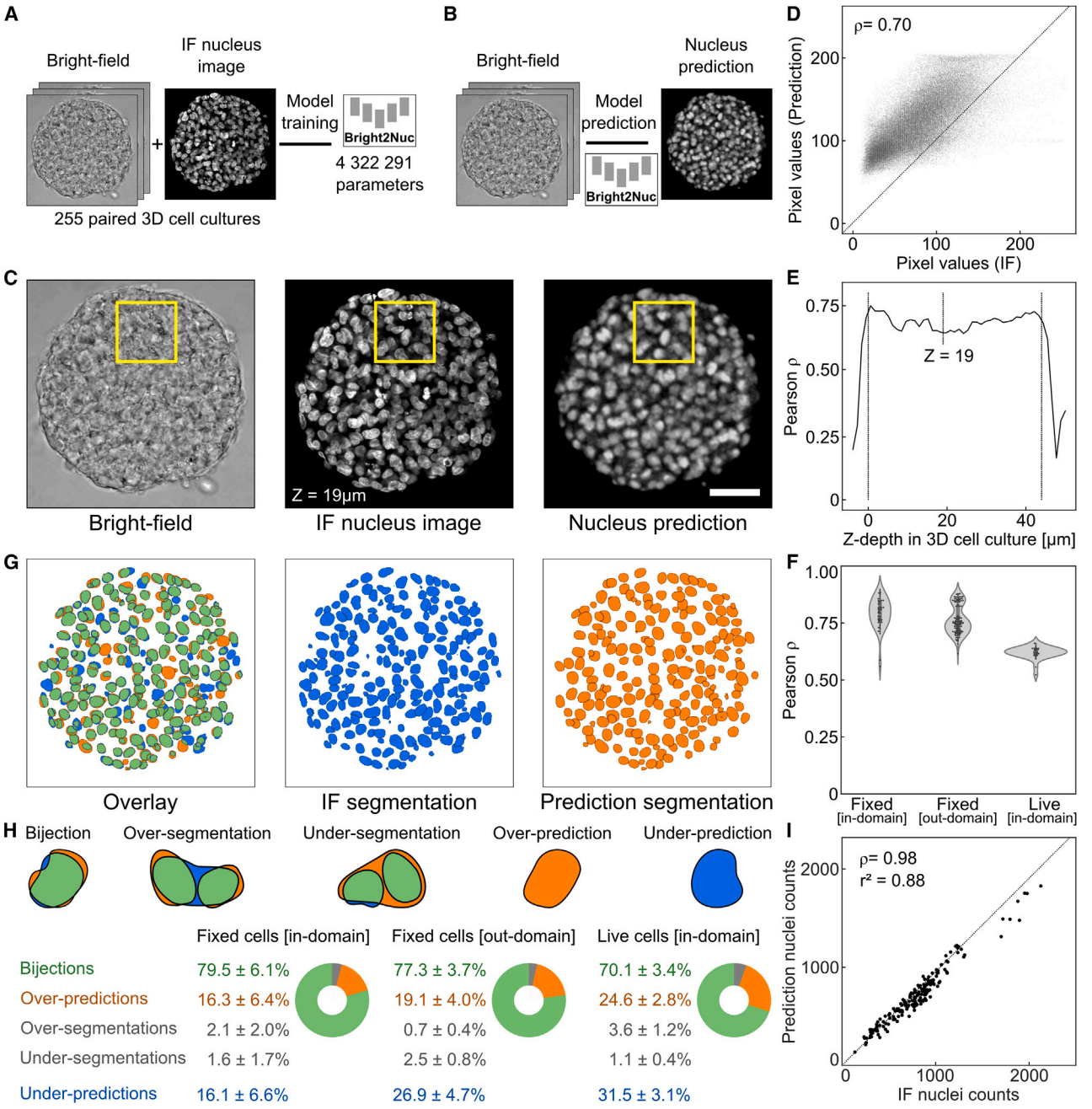

Figure 2. Neural network accurately predicts nuclear staining in 3D cell cultures from bright-field images

(A) We trained Bright2Nuc, a U-Net-based neural network, on paired bright-field and immunofluorescence (IF) nucleus images.

(B) We used it to predict nucleus images from bright-field images. The model considers three consecutive Z slices of the 3D bright-field image to output each Z slice of the nucleus prediction.

(C) Representative bright-field image of an on-chip 3D cell culture (left), corresponding ground-truth DAPI IF nucleus image (middle), and the predicted nucleus image (right). Yellow rectangles highlight the position of a specific region for comparison. Scale bar: 100 µm.

(D) Correlation between the fluorescence pixel values of the ground truth nucleus image given in (C) and the pixel values of the corresponding predicted nucleus image (Pearson correlation $\rho = 0.70$). Each data point represents a single pixel value, and the line represents the y = x identity.

(E) The model's prediction performance is independent of the imaging depth. The Pearson correlation between the predicted and ground-truth pixels was stable along the z axis of the cell culture shown in (C).

(F) Average Pearson correlation between the ground-truth and predicted pixel values from whole 3D cell cultures imaged in either the fixed or live state. In domain refers to the images coming from the in-domain test set, which are images extracted from the same experiments as the images used for Bright2Nuc model training but excluded from the training itself. Out domain refers to images extracted from experiments completely independent of the model training. Average

(legend continued on next page)

and out-domain (ρ = 0.76 ± 0.06, N = 123) images (Figure 2F.). Furthermore, we assessed the robustness of the model by varying the illumination parameters on a subset of 31 cell cultures in an out-domain experiment. The correlations did not change when imaged with either a 555 or 633 nm laser wavelength (ρ = 0.77 ± 0.06 for λ = 555 nm, ρ = 0.76 ± 0.06 for λ = 633 nm, N = 31 fixed out-domain cultures; Figure S2A). Finally, an ablation study was conducted to estimate the number of images required to train a high-performance Bright2Nuc model. To this end, we retrained Bright2Nuc models on randomly selected subsamples of the training data (2%, 5%, 10%, 25%, and 50% of the N = 255 3D cell cultures). The results showed that using 10% of the total training data (i.e., N = 25 3D cell cultures) was sufficient to achieve similar performance as using the full dataset (Figure S2B).

Segmentation of nuclei from bright-field imaging

To segment Bright2Nuc-predicted nucleus images, we retrained StarDist[14,15] with fluorescence images from the same training dataset as for Bright2Nuc (see experimental procedures). First, we compared the *in silico* segmentation results for the predicted nucleus images with the *in silico* segmentation results for the immunofluorescent nucleus images (Figure 2G). Secondly, we compared the *in silico* segmentation results with manually annotated images of a 3D cell culture from an in-domain fixed test set. This 3D cell culture was excluded from the training sets of both Bright2Nuc and StarDIst models. We found that the quality of the *in silico* segmented ground truth was high with low variation compared with the manually segmented results (96.8% of bijections between manual and *in silico* ground truths and only 5.9% of under-predictions; Figures S2C–S2E), confirming the robustness of the *in silico* segmentation approach. Further, to benchmark the segmentations on the predicted images, segmented nuclei were classified into five categories: (1) bijections, that is, predicted nuclei overlapping with a single nucleus in the ground truth image; (2) over-segmentations, that is, two or more predicted nuclei overlapped with a single nucleus in the ground-truth image; (3) under-segmentations, that is, single predicted nuclei overlapped with two or more nuclei in the ground-truth image; (4) over-predictions, where predicted nuclei overlapped with no nuclei in the ground-truth image; and (5) under-predictions, where nuclei in the ground truth existed with no overlap in the prediction image (Figure 2H). For in-domain fixed cultures, the Bright2Nuc and StarDist approach resulted in 79.5% ± 6.1% of the predicted nuclei as bijections (mean ± SD, N = 54 cultures). An additional 2.1% ± 2% and 1.6% ± 1.7% of the nuclei were predicted correctly but were over- or under-segmented, respectively. However, the approach also yielded 16.3% ± 6.4% of over-predictions, whereas conversely, 16.1% ± 6.6% of all ground-truth segmentations were under-predicted (Figure 2H). Nuclei segmentation from bright-field predictions was also achieved in in-domain live cell cultures at the cost of a slightly decreased accuracy of 70.1% ± 3.4% of bijections (N = 31) (Figure 2H). Furthermore, the approach yielded similar results for out-domain fixed images with a percentage of 77.3% ± 3.7% of bijections (N = 123). Notably, this approach yielded a higher percentage of over- and under-predictions; however, we adjusted the detection threshold of the StarDist segmentation model to optimize the nuclei count accuracy. In fact, under- and over-predictions compensate for each other and result in high accuracy for predicting the number of nuclei in 3D cell cultures from both in and out domains, fixed or live, when compared with the *in silico* ground-truth count (Figure 2I; ρ = 0.98; r^2 = 0.88).

Label-free prediction of differentiation state

Next, we investigated whether morphological and other features derived from bright-field images were predictive of hiPSC differentiation. In previous studies, the morphology of stem cell nuclei was shown to be indicative of their differentiation state.[17–20] Therefore, we first mapped the expression of the three TFs to a single normalized value: the differentiation label (DL). The DL was defined as the ratio between the average of the normalized expressions of e_{FOXA2} and e_{SOX17} of the differentiation markers FOXA2 and SOX17 and the sum of the normalized expression of e_{OCT4} of the pluripotency marker OCT4 and the differentiation markers:

$$DL = \frac{1}{1+\frac{2e_{OCT4}}{e_{FOXA2}+e_{SOX17}}}$$

DL progressed from values close to zero for pluripotent cells at t = 0 h with high OCT4 expression to a value of ~1 for DE cells after 72 h with high FOXA2 and SOX17 expression (Figure S3). To predict the DL for each nucleus, we designed an explainable feature-based approach. For each of the 26,213 segmented nuclei along the DE differentiation trajectory, 120 features were extracted: 64 morphological features from the 3D segmentations after Bright2Nuc and StarDist applications, and 56 bright-field texture features were extracted from a fixed-sized bounding box centered on the nucleus on the paired bright-field 3D images. A random forest algorithm with 1,000 estimators and a depth of 10 was trained on the features for predicting DL (experimental procedures). The ground-truth DL for model training was calculated for each nucleus from the TF expression in the bounding box of the associated IF image (Figure 3A).

The resulting random forest model predicted single-cell DL in the bright-field images of 3D cell cultures fixed along the DE

Pearson correlations were ρ = 0.79 ± 0.07 for fixed in-domain cultures (mean ± SD, N = 54 cultures), ρ = 0.76 ± 0.07 for fixed out-domain cultures (N = 123), and ρ = 0.62 ± 0.03 for live in-domain cultures (N = 31).

(G) 3D *in silico* segmentation using StarDist of the IF nucleus image in (C) (middle, blue) and the predicted nucleus image (right, orange). The overlays of both segmentations show a high overlap (left, green; 80.6% overlapping area with the *in silico* segmentation).

(H) Top: categories used for comparing the predicted segmentation to the *in silico* IF segmentation. Bottom: distribution of categories for predicted segmentations from fixed (in-domain) (N = 54), fixed (out-domain) (N = 123), and live (in-domain) (N = 31) 3D cell cultures.

(I) High accuracy for the prediction of nuclei counts in the 85 fixed and live 3D cell cultures in the in-domain test set and the 123 out-domain fixed cultures (Pearson correlation ρ = 0.98; coefficient of determination r^2 = 0.88). The diagonal line represents the y = x identity.

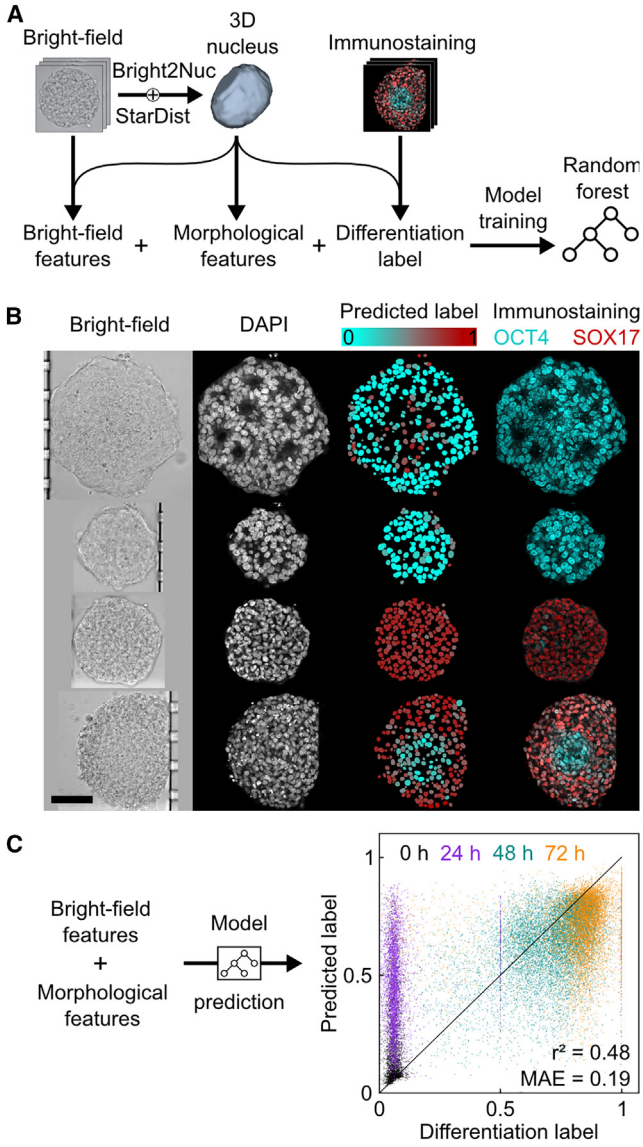

Figure 3. Bright-field and predicted morphological features predict single-cell differentiation state

(A) We extracted 56 features from bright-field and 63 morphological features from segmented Bright2Nuc 3D images in combination with the differentiation label obtained from the IF expression to train the random forest model.

(B) Visually, the predicted label (3rd column, color coded from cyan to red) matches the true IF expression (last column, merged IF images showing OCT4 in cyan and SOX17 in red). Scale bar: 100 μm. The random forest model predicted a differentiation label for each cell in the on-chip 3D cell cultures.

(C) Comparison of the ground-truth with the predicted differentiation label is shown on the right. Each data point represents a single nucleus (N = 26,213) extracted from 49 3D cell cultures. (r^2 = 0.48, mean absolute error = 0.19). The mean absolute error observed on nuclei in 3D cell cultures fixed 24 h after the start of definitive endoderm (DE) differentiation is much higher (mean absolute error $[MAE]_{24h}$ = 0.38 ± 0.18, n = 4,376) than the one for other time points (MAE_{0h} = 0.15 ± 0.18, n = 3,028; MAE_{48h} = 0.13 ± 0.11, n = 11,364; MAE_{72h} = 0.17 ± 0.14, n = 7,445). This discrepancy can be explained by the inaccurate value of the differentiation label obtained from the IF images. At 24 h, cells displayed high OCT4 and low FOXA2/SOX17 expression, thus resulting in low differentiation label values, even though the cells were already committed to the DE differentiation path. The random forest interestingly predicts a label value of DL_{24h}-pred = 0.46 ± 0.18, which spans the range between the values for the 0 and 48 h time points (DL_{0h}-pred = 0.21 ± 0.18; DL_{48h}-pred = 0.64 ± 0.15).

differentiation trajectory. In a round-robin fashion, five random forest models were trained on different training and test sets, ensuring that each cell culture was contained in the test set exactly once, while the training and test sets were split on the level of whole-cell cultures. Visually, the predicted DL correlated with true IF staining, even in the case of non-homogeneously expressing cell cultures (Figure 3B). For all 26,213 nuclei, the predicted DL correlated with the true DL with a coefficient of determination of r^2 = 0.48 and a mean absolute error of 0.19 ± 0.17 (mean ± SD; Figure 3C). We observed strong deviations for nuclei fixed 24 h after DE induction where the mean absolute error was higher than that at other time points. Interestingly, the predicted DL values at 24 h spanned the entire range, indicating that the random forest predicted nuclei as being in a developmental transition state rather than resembling pure DE or pluripotent cell states. The discrepancy between the predicted and true DLs can be explained by an inaccurate ground truth at 24 h, where cells exhibited a high OCT4 and a low FOXA2/SOX17 expression (Figures 1D and 1E), resulting in a low true DL (0.09 ± 0.14, mean ± SD, n = 4,376) indicative of pluripotent cells, which does not reflect the state of those cells after 24 h of DE induction.

In fact, a single-cell transcriptomic time trajectory of DE differentiation under comparable conditions[21] showed that after 24 h, the transcriptome of hiPSCs changed differently from PSCs while still expressing *OCT4* at the mRNA level (Figure S4). Consequently, the simplified view of cell type differentiation based on single-cell state fluorescence markers argues for descriptive states, whereas the neural network learning approach resolves a continuous cell type transition as is seen with time-resolved single-cell transcriptomics. By evaluating the feature importance of the random forest model, we found that features calculated on the bright-field images contributed 66% to the prediction, with the highest weighted feature being the SD of the pixel values of the bright-field image (Table S1). Our approach highlights the rich and hidden information sources of bright-field images and their potential to resolve the transcriptional states of human stem cells.

Label-free tracking of single cells

Bright2Nuc can bridge the domain gap between fixed and living tissues by tracking nuclei in live 3D cell cultures. To this end, we first generated surrogate *in silico* ground-truth tracking data with 3D cell cultures formed from a mixture of wild-type hiPSCs and the SOX2-T2A-tdTomato reporter line in a 1:2 ratio to generate heterogeneous mixtures of labeled and non-labeled nuclei. Bright-field and IF images were acquired every 7.5 min for 17 h, resulting in 136 frames (Video S2). The trained Bright2Nuc was then applied to every frame of the bright-field image sequence to predict nuclei. Predicted and IF-stained nuclei, which we take here assign as *in silico* ground truth, were tracked using TrackMate.[22] Expectedly, we detected roughly two-thirds of the number of nuclei (Figure 4A, blue curve) in the IF images

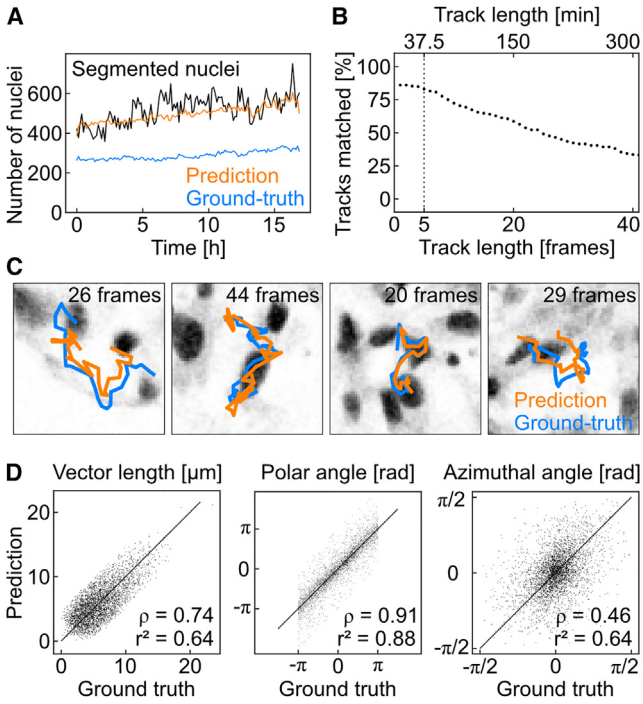

Figure 4. Label-free single-cell tracking in live 3D cell cultures

(A) Tracked nuclei in the label-free predicted images (orange) and fluorescence reporter images (blue) in one representative 3D cell culture. As per the ratio of fluorescent cells to the wild type, the *in silico* ground truth contained fewer tracks than the prediction. Incorporating temporal information by counting the number of tracks results in a more stable nucleus count than that based on the segmentations of each individually segmented label-free predicted image (black).

(B) If we require the tracks to match for a higher number of frames, the percentage of tracks in the fluorescence reporter images with a matched track in the predicted images decreases. The longer we require the tracks to be, the fewer we can identify as matching.

(C) Representative 3D single-cell tracks in the predicted nucleus images (orange) and *in silico* ground-truth SOX2-T2A-tdTomato fluorescence nucleus reporter images (blue). The background gray-value images show the *in silico* ground-truth nuclear signal at the tracking end. The frame interval is 7.5 min.

(D) In spherical coordinates averaged over five frames, we found a high correlation in displacement (vector length, $\rho = 0.74$, $r^2 = 0.64$) and directionality (polar angle, $\rho = 0.91$, $r^2 = 0.88$, and azimuthal angle, $\rho = 0.46$, $r^2 = 0.64$) and between prediction and *in silico* ground truth.

compared with nuclei from the predicted images (Figure 4A, black curve). With increasing experimental time, the number of detected tracks increased due to cell proliferation in both curves, with the ratio between *in silico* ground-truth and predicted tracks remaining constant at $n_{GT}/n_{Pred} = 0.58 \pm 0.03$ (Figure 4A; mean ± SD, n = 136 frames). Assigning nuclei to tracks resulted in a more stable nuclei count than counting segmented nuclei alone (Figure 4A, orange curve). Tracks in the *in silico* ground truth are, on average, longer than tracks found in the predicted sequence (Figure S5), which can be due to under-predictions of Bright2Nuc (Figure 2), causing nuclei to be lost in a track.

For further tracking evaluation, we calculated the percentage of *in silico* ground-truth tracks with a matched predicted track as a function of the predicted track length (Figure 4B). We counted a match between two tracks if the distance between the center of mass of nuclei in the *in silico* ground-truth and predicted images was less than 11 µm, which is roughly equal to the average nuclei diameter. The percentage of matched tracks decreased steadily from an initial 85% for the minimum requirement of two frames to approximately 50% for the requirement of 25 consecutive frames, corresponding to 3 h of imaging (Figure 4B).

Finally, we compared tracks from the *in silico* ground truth with their matched predicted tracks, taking an arbitrary threshold of five consecutive frames, for which 81% of the *in silico* ground-truth tracks had a predicted track match (Figure 4B). Exemplary velocity vectors were derived by averaging the cell movement over five consecutive frames matched visually (Figure 4C), and their spherical coordinates were correlated between the *in silico* ground-truth and predicted tracks with Pearson correlations for the vector lengths, polar angles, and azimuthal angles of ρ = 0.74, 0.91, and 0.46, respectively (Figure 4D). The distributions of both the *in silico* ground-truth and predicted velocity vector coordinates were similar (Figures S5D–S5F). Movement in the xy plane was isotropic with a homogeneous distribution of the polar angle (Figure S5E), whereas the values of the azimuthal angle remained close to 0 (Figure S5F), indicating little movement in the z direction. The limited z-directed movement was probably caused by the constrained geometry of the on-chip cultures. However, this confinement did not affect nuclei velocities, as evidenced by the lack of dependence of the velocity vector length on the z position of the nuclei (Figure S5C). Overall, considering a track length of five frames, Bright2Nuc coupled with the TrackMate algorithm allowed us to track 81% of the nuclei in 3D cell culture (Figure 4C).

Label-free detection of cell velocities during differentiation

During DE differentiation, hPSCs undergo synchronous epithelial-mesenchymal transition (EMT).[23–25] It is known that DE cells show significantly higher migration in 2D experiments compared with pluripotent cells in a scratch assay,[23] which argues that DE cells exhibit higher cell mobility than stem cells. Therefore, in the last step, we investigated whether Bright2Nuc in combination with single-nuclei tracking can detect motility changes in label-free 3D cell cultures during DE differentiation. Along this line, we detected changes in the expression of cell adhesion molecules indicative of EMT during the DE differentiation on chip (Figure 5A). IF images of fixed 3D cell cultures along the DE differentiation trajectory showed that epithelial-cadherin (E-CAD)/neural-cadherin (N-CAD) expression changes co-occurred with upregulation of the DE marker SOX17. The single-cell transcriptomic dataset[21] also confirmed EMT TF changes, such as SNAIL1/2, whose expression peaked between the 24 and 48 h time points (Figure S4). To assess changes in cell motility during DE differentiation, we captured bright-field movies of six 3D cell cultures every 24 h over 75 min with a 5 min/frame acquisition period (Figure 5). Bright-field images were acquired using confocal microscopy with the same resolution as before. The Bright2Nuc + TrackMate approach was then used to extract the nuclei velocities, defined as the effective displacement of the nuclei over five frames (Figure 5A). Strikingly, we observed an

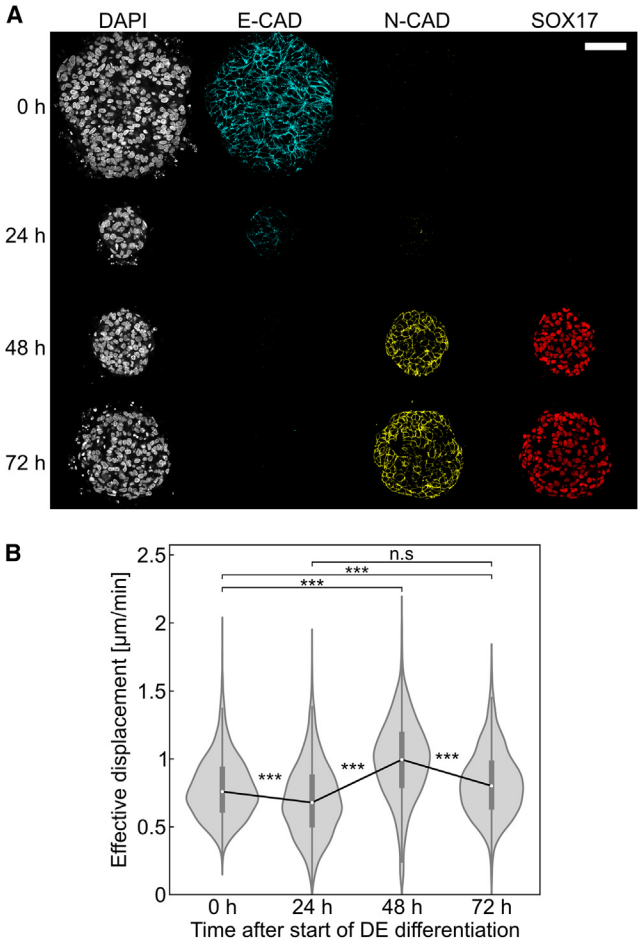

Figure 5. Single-cell live tracking in 3D cell cultures during DE differentiation captures increased cell mobility

(A) A significant increase in effective displacement correlates with the change in cadherin expression, as shown in the IF confocal images of 3D cell cultures fixed along the DE differentiation trajectory, showing the evolution of epithelial-cadherin (E-CAD) and neural-cadherin (N-CAD) expression. The evolution of the differentiation marker SOX17 was shown to mark progress toward the DE stage. Scale bar: 100 µm.

(B) Distribution of the effective displacement over five frames, calculated using Bright2Nuc and TrackMate on bright-field movies with a 24 h interval along the DE differentiation trajectory. Each time point represents the distribution of the velocity vectors of nuclei in six 3D cell cultures (number of nuclei: N_{0h} = 2,862, N_{24h} = 1,308, N_{48h} = 2,144, and N_{72h} = 2,820). Movies were acquired with a 5 min per frame interval of over 75 min. White circles indicate the mean, boxes mark the first and third quartiles, and bars indicate the standard deviation. For significance testing a Mann-Whitney U test was perfromed (ns. > 0.05, *p < 0.05, **p < 0.01, ***p < 0.001).

increase in effective cell displacement up to 48 h after induction of the DE differentiation. The highest effective cell displacement (D_{48h} = 0.98 ± 0.30 µm/min, mean ± SD) coincided with the time point of the E-CAD/N-CAD expression change and the appearance of the DE-specific marker SOX17. The population median of the four effective cell displacement distributions (D_{0h} = 0.78 ± 0.22 µm/min, D_{24h} = 0.70 ± 0.26 µm/min, D_{48h} = 0.98 ± 0.30 µm/min, D_{72h} = 0.82 ± 0.24 µm/min, mean ± SD) differs significantly ($p = 3.9 \times 10^{-242}$, Kruskal-Wallis H test). Post hoc analysis with a Bonferroni correction revealed a significant increase at the 48 h time point compared with the other time points ($p_{0–48h} = 7.3 \times 10^{-165}$, $p_{24–48h} = 1.4 \times 10^{-164}$, $p_{48–72h} = 2.3 \times 10^{-109}$, Mann-Whitney U test). Thus, the cells displayed higher motility during DE differentiation than during the pluripotent state. Notably, cell movements within the 3D cell cultures were non-directed throughout differentiation, as evidenced by the homogeneously low values of directionality calculated from the same velocity vectors. Interestingly, the measured increase in cell migration rates during DE differentiation was lower than that previously reported in 2D cultures,[23] where DE cells showed a five times higher migration rate than that of pluripotent cells. This could reflect the more complex extracellular matrix (ECM) within the 3D cell culture compared with a simple 2D cell surface culture.

DISCUSSION

Microfluidic cell culture technologies for controlling the massive parallelization of 3D cell cultures are rapidly advancing, while high-throughput analytical methods to exploit miniaturized biological samples are lacking. In this study, we provide a label-free and live imaging approach to cope with the faster image acquisition of on-chip-cultivated 3D stem cell cultures. The developed neural network learning algorithm, Bright2Nuc, can be coupled with pre-existing image analysis tools such as StarDist and TrackMate for segmentation and tracking, respectively. With StarDist, Bright2Nuc enabled us to infer the cell number and nuclear locations from accessible confocal bright-field images with an accuracy of over 80% for 3D cell cultures with more than 10,000 cells. Using the simplest imaging methods for high-content imaging, we offer a general imaging approach for screening 3D tissues. Deep learning approaches to detect cell nuclei have been previously employed for 2D adherent cell cultures[8,9,11,12] or histological tissue slices.[10] Existing neural networks have not yet attempted to infer information from cell images acquired with lower numerical aperture objectives and xy resolution[9–11] in 3D. Beyond locating only the nucleus volume and positions, morphological features from inferred nuclei and corresponding bright-field images allowed the determination of transcriptional cell states along the pluripotent-to-DE differentiation trajectory. Notably, the resulting cell state predictions were more continuous than the cell state descriptions generated from the fluorescence signals of descriptive fluorescence markers, which is the standard research approach in developmental biology. Our results highlight the currently untapped potential information contained in the bright-field images.

In addition to the static view, we demonstrated that Bright2Nuc can resolve real-time information from live nuclei in 3D cell cultures by using a neural network together with the TrackMate algorithm. For example, we captured label-free cell dynamics, indicating EMT on a timescale of hours. The homogeneous transition from pluripotent to DE cell stage within the on-chip-cultivated 3D cell culture was reflected in the nuclei velocity changes during differentiation.

Limitations of the study

One limitation of our study is the limited or missing ground-truth data for cell segmentation and cell tracking, respectively.

Although we manually segmented six 3D cell cultures, the large-scale benchmarking of segmentations in Bright2Nuc images was performed using *in-silico*-generated ground-truth data. Nevertheless, the Pearson correlation coefficients between the segmented Bright2Nuc images and *in-silico*-generated ground-truth data were comparable to those of the sparse manually generated ground truth, which argues for the applicability of our approach. The generation of complete manually annotated cell tracks for 3D cell cultures with over 400 cells per frame over 136 frames is challenging. However, here, the surrogated *in silico* ground-truth data generated from fluorescence images of an iSPC reporter cell line with labeled nuclei showed a high correlation with the tracking results obtained from the Bright2Nuc images, demonstrating that the accuracy of our tracking approach was comparable to using fluorescence images from labeled cells or organelles. So far, Bright2Nuc was only tested on images taken under the given constraints in terms of the used image acquisition microenvironment and microscope equipment. The application of Bright2Nuc to other imaging modalities remains to be shown. Our ablation study showed that 10 s of 3D cell culture was sufficient to train Bright2Nuc successfully, limiting the time required to provide annotated training data for future experiments. Within our working range, Bright2Nuc allowed for the assessment of motion directionality, cell migration, and neighboring cell-cell contacts upon the formation of architectural structures in the endodermal tissue. This can be directly extended to resolve more complex tissue formations such as those fully developing into pancreatic or liver cell types. To further decrease the image acquisition time and increase the time resolution for subsequent 3D cell culture, we expect Bright2Nuc to be adopted for wide-field bright-field images. In summary, we believe that the general framework of Bright2Nuc opens a diverse field of applications for dynamic high-content screening of 3D cell cultures on chips.

STAR★METHODS

Detailed methods are provided in the online version of this paper and include the following:

- KEY RESOURCES TABLE
- RESOURCE AVAILABILITY
  - Lead contact
  - Materials availability
  - Data and code availability
- EXPERIMENTAL MODEL AND STUDY PARTICIPANT DETAILS
- METHOD DETAILS
  - Microfluidic chip fabrication
  - Microfluidic chip operations
  - Definitive endoderm differentiation
  - Immunocytochemistry on-chip
  - Image acquisition
  - Fluorescence signal correction
  - *In silico* nuclear staining
  - Nuclei segmentation
  - Transcription factor expression prediction
  - Live cell tracking
  - Single-cell analysis
- QUANTIFICATION AND STATISTICAL ANALYSIS

SUPPLEMENTAL INFORMATION

Supplemental information can be found online at https://doi.org/10.1016/j.crmeth.2023.100523.

ACKNOWLEDGMENTS

We thank Fabian Theis, Henrik Semb, Sophia Wagner, Melanie Schulz, Benedikt Mairhörmann, and Valerio Lupperger for their discussions and ideas. C.M. and M.M. received funding from the European Research Council (ERC) under the European Union's Horizon 2020 research and innovation program with grant agreement nos. 866411 and 772646, respectively. This work was funded by the Helmholtz Pioneer Campus. S.S.B. has received funding from F. Hoffmann-La Roche (no grant number applicable) and is supported by the Helmholtz Association under the joint research school "Munich School for Data Science - MUDS." C.M. acknowledges support from the Hightech Agenda Bayern.

AUTHOR CONTRIBUTIONS

S.A. cultured, stained, and imaged the cell lines. D.J.E.W. implemented the code, trained the models, and performed the computational experiments. S.A. and D.J.E.W. evaluated the experiments, designed the figures, and wrote the manuscript with C.M. and M.M. D.J.E.W. and S.S.B. developed a Bright2Nuc Python package. C.M. and M.M. supervised this study.

DECLARATION OF INTERESTS

The authors declare no competing interests.

Received: October 26, 2022
Revised: May 9, 2023
Accepted: June 15, 2023
Published: July 13, 2023

REFERENCES

1. Avior, Y., Sagi, I., and Benvenisty, N. (2016). Pluripotent stem cells in disease modelling and drug discovery. Nat. Rev. Mol. Cell Biol. *17*, 170–182. https://doi.org/10.1038/nrm.2015.27.
2. Takahashi, Y., Takebe, T., and Taniguchi, H. (2016). Engineering pancreatic tissues from stem cells towards therapy. Regen. Ther. *3*, 15–23. https://doi.org/10.1016/j.reth.2016.01.002.
3. Zhao, X., Zhu, Y., Laslett, A.L., and Chan, H.F. (2020). Hepatic Differentiation of Stem Cells in 2D and 3D Biomaterial Systems. Bioeng *7*, 47. https://doi.org/10.3390/bioengineering7020047.
4. Liu, Y., and Chen, Y.-G. (2018). 2D- and 3D-Based Intestinal Stem Cell Cultures for Personalized Medicine. Cells *7*, 225. https://doi.org/10.3390/cells7120225.
5. Luni, C., Gagliano, O., and Elvassore, N. (2022). Derivation and Differentiation of Human Pluripotent Stem Cells in Microfluidic Devices. Annu. Rev. Biomed. Eng. *24*, 231–248. https://doi.org/10.1146/annurev-bioeng-092021-042744.
6. Lukonin, I., Zinner, M., and Liberali, P. (2021). Organoids in image-based phenotypic chemical screens. Exp. Mol. Med. *53*, 1495–1502. https://doi.org/10.1038/s12276-021-00641-8.
7. Nie, J., and Hashino, E. (2017). Organoid technologies meet genome engineering. EMBO Rep. *18*, 367–376. https://doi.org/10.15252/embr.201643732.
8. Lee, G., Oh, J.-W., Her, N.-G., and Jeong, W.-K. (2021). DeepHCS + + : Bright-field to fluorescence microscopy image conversion using multi-task learning with adversarial losses for label-free high-content screening.

Med. Image Anal. *70*, 101995. https://doi.org/10.1016/j.media.2021.101995.

9. Christiansen, E.M., Yang, S.J., Ando, D.M., Javaherian, A., Skibinski, G., Lipnick, S., Mount, E., O'Neil, A., Shah, K., Lee, A.K., et al. (2018). Silico Labeling: Predicting Fluorescent Labels in Unlabeled Images. Cell *173*, 792–803.e19. https://doi.org/10.1016/j.cell.2018.03.040.
10. Rivenson, Y., Liu, T., Wei, Z., Zhang, Y., de Haan, K., and Ozcan, A. (2019). PhaseStain: the digital staining of label-free quantitative phase microscopy images using deep learning. Light Sci. Appl. *8*, 23. https://doi.org/10.1038/s41377-019-0129-y.
11. Ounkomol, C., Seshamani, S., Maleckar, M.M., Collman, F., and Johnson, G.R. (2018). Label-free prediction of three-dimensional fluorescence images from transmitted-light microscopy. Nat. Methods *15*, 917–920. https://doi.org/10.1038/s41592-018-0111-2.
12. Kandel, M.E., He, Y.R., Lee, Y.J., Chen, T.H.-Y., Sullivan, K.M., Aydin, O., Saif, M.T.A., Kong, H., Sobh, N., and Popescu, G. (2020). Phase imaging with computational specificity (PICS) for measuring dry mass changes in sub-cellular compartments. Nat. Commun. *11*, 6256. https://doi.org/10.1038/s41467-020-20062-x.
13. Unger, M.A., Chou, H.P., Thorsen, T., Scherer, A., and Quake, S.R. (2000). Monolithic microfabricated valves and pumps by multilayer soft lithography*288* (Science), pp. 113–116.
14. Schmidt, U., Weigert, M., Broaddus, C., and Myers, G. (2018). Medical Image Computing and Computer Assisted Intervention – MICCAI 2018, 21st International Conference, Granada, Spain, September 16-20, 2018, Proceedings, Part II. Lect. Notes Comput. Sci., 265–273. https://doi.org/10.1007/978-3-030-00934-2_30.
15. Weigert, M., Schmidt, U., Haase, R., Sugawara, K., and Myers, G. (2020). Star-convex Polyhedra for 3D Object Detection and Segmentation in Microscopy. 2020. Ieee Winter Conf Appl Comput Vis Wacv *00*, 3655–3662. https://doi.org/10.1109/wacv45572.2020.9093435.
16. Ardila Riveros, J.C., Blöchinger, A.K., Atwell, S., Moussus, M., Compera, N., Rajabnia, O., Georgiev, T., Lickert, H., and Meier, M. (2021). Automated optimization of endoderm differentiation on chip. Lab Chip *21*, 4685–4695. https://doi.org/10.1039/d1lc00565k.
17. Orozco-Fuentes, S., Neganova, I., Wadkin, L.E., Baggaley, A.W., Barrio, R.A., Lako, M., Shukurov, A., and Parker, N.G. (2019). Quantification of the morphological characteristics of hESC colonies. Sci. Rep. *9*, 17569. https://doi.org/10.1038/s41598-019-53719-9.
18. McColloch, A., Rabiei, M., Rabbani, P., Bowling, A., and Cho, M. (2019). Correlation between Nuclear Morphology and Adipogenic Differentiation: Application of a Combined Experimental and Computational Modeling Approach. Sci. Rep. *9*, 16381. https://doi.org/10.1038/s41598-019-52926-8.
19. Heo, S.-J., Driscoll, T.P., Thorpe, S.D., Nerurkar, N.L., Baker, B.M., Yang, M.T., Chen, C.S., Lee, D.A., and Mauck, R.L. (2016). Differentiation alters stem cell nuclear architecture, mechanics, and mechano-sensitivity. Elife *5*, e18207. https://doi.org/10.7554/elife.18207.
20. Ankam, S., Teo, B.K.K., Pohan, G., Ho, S.W.L., Lim, C.K., and Yim, E.K.F. (2018). Temporal Changes in Nucleus Morphology, Lamin A/C and Histone Methylation During Nanotopography-Induced Neuronal Differentiation of Stem Cells. Front. Bioeng. Biotechnol. *6*, 69. https://doi.org/10.3389/fbioe.2018.00069.
21. Cuomo, A.S.E., Seaton, D.D., McCarthy, D.J., Martinez, I., Bonder, M.J., Garcia-Bernardo, J., Amatya, S., Madrigal, P., Isaacson, A., Buettner, F., et al. (2020). Single-cell RNA-sequencing of differentiating iPS cells reveals dynamic genetic effects on gene expression. Nat. Commun. *11*, 810. https://doi.org/10.1038/s41467-020-14457-z.
22. Tinevez, J.-Y., Perry, N., Schindelin, J., Hoopes, G.M., Reynolds, G.D., Laplantine, E., Bednarek, S.Y., Shorte, S.L., and Eliceiri, K.W. (2017). TrackMate: An open and extensible platform for single-particle tracking. Methods *115*, 80–90. https://doi.org/10.1016/j.ymeth.2016.09.016.
23. Li, Q., Hutchins, A.P., Chen, Y., Li, S., Shan, Y., Liao, B., Zheng, D., Shi, X., Li, Y., Chan, W.-Y., et al. (2017). A sequential EMT-MET mechanism drives the differentiation of human embryonic stem cells towards hepatocytes. Nat. Commun. *8*, 15166. https://doi.org/10.1038/ncomms15166.
24. D'Amour, K.A., Agulnick, A.D., Eliazer, S., Kelly, O.G., Kroon, E., and Baetge, E.E. (2005). Efficient differentiation of human embryonic stem cells to definitive endoderm. Nat. Biotechnol. *23*, 1534–1541. https://doi.org/10.1038/nbt1163.
25. Tauran, Y., Poulain, S., Lereau-Bernier, M., Danoy, M., Shinohara, M., Segard, B.-D., Kato, S., Kido, T., Miyajima, A., Sakai, Y., et al. (2019). Analysis of the transcription factors and their regulatory roles during a step-by-step differentiation of induced pluripotent stem cells into hepatocyte-like cells. Mol. Omics *15*, 383–398. https://doi.org/10.1039/c9mo00122k.
26. Hohwieler, M., Illing, A., Hermann, P.C., Mayer, T., Stockmann, M., Perkhofer, L., Eiseler, T., Antony, J.S., Müller, M., Renz, S., et al. (2017). Human pluripotent stem cell-derived acinar/ductal organoids generate human pancreas upon orthotopic transplantation and allow disease modelling. Gut *66*, 473–486. https://doi.org/10.1136/gutjnl-2016-312423.
27. Shahryari, A., Moya, N., Siehler, J., Wang, X., Burtscher, I., and Lickert, H. (2021). Increasing Gene Editing Efficiency for CRISPR-Cas9 by Small RNAs in Pluripotent Stem Cells. Crispr J *4*, 491–501. https://doi.org/10.1089/crispr.2021.0014.
28. Zhu, Z., Li, Q.V., Lee, K., Rosen, B.P., González, F., Soh, C.-L., and Huangfu, D. (2016). Genome Editing of Lineage Determinants in Human Pluripotent Stem Cells Reveals Mechanisms of Pancreatic Development and Diabetes. Cell Stem Cell *18*, 755–768. https://doi.org/10.1016/j.stem.2016.03.015.
29. Ronneberger, O., Fischer, P., and Brox, T. (2015). U-Net: Convolutional Networks for Biomedical Image Segmentation. Preprint at Arxiv. https://doi.org/10.48550/arxiv.1505.04597.
30. Waibel, D.J.E., Shetab Boushehri, S., and Marr, C. (2021). InstantDL: an easy-to-use deep learning pipeline for image segmentation and classification. BMC Bioinf. *22*, 103. https://doi.org/10.1186/s12859-021-04037-3.
31. Varoquaux, G., Buitinck, L., Louppe, G., Grisel, O., Pedregosa, F., and Mueller, A. (2015). Scikit-learn: Machine Learning Without Learning the Machinery. Getmobile Mob Comput Commun *19*, 29–33. https://doi.org/10.1145/2786984.2786995.
32. McKinney, W. (2010). Data Structures for Statistical Computing in Python. Proc 9th Python Sci Conf, 56–61. https://doi.org/10.25080/majora-92bf1922-00a.

STAR★METHODS

KEY RESOURCES TABLE

REAGENT or RESOURCE	SOURCE	IDENTIFIER
Antibodies		
anti-OCT4	Cell Signaling	Cat#75463; RRID: AB_2799870
anti-FOXA2	Cell Signaling	Cat#8186S; RRID: AB_10891055
anti-SOX17	Acris/Novus	Cat#GT15094; RRID: AB_1623027
anti-N-Cadherin	BD	Cat#610920; RRID: AB_2077527
anti-E-Cadherin	Cell Signaling	Cat#3195S; RRID: AB_2291471
anti-Mouse	Invitrogen	Cat#A21202; RRID: AB_141607
anti-Rabbit	Invitrogen	Cat#A31572; RRID: AB_162543
anti-Goat	Invitrogen	Cat#A21082; RRID: AB_2535739
anti-Mouse	Dianova	Cat#715-175-151; RRID: AB_2619678
anti-Goat	Invitrogen	Cat#A11055; RRID: AB_2534102
Chemicals, peptides, and recombinant proteins		
ActA	Peprotech	Cat# 120-14-300
CHIR99021, GSK3β inhibitor	Tebu-bio	Cat# 24804-0004
ROCK inhibitor, Y-27632	Santa Cruz Biotechnology	Cat# sc-281642A
MCDB131	Gibco®	Cat# 10372-019
Glutamax	Life Technologies	Cat# 35050-079
BSA	Sigma Aldrich	Cat# 10775835001
Sodium bicarbonate	Sigma Aldrich	Cat# S6297
Glucose	Sigma Aldrich	Cat# G8769
ITS-X	Life Technologies	Cat# 51500-056
Ascorbic acid	Sigma-Aldrich	Cat# A4544
Penicillin/Streptomycin	Gibco®	Cat# 15140-122
Deposited data		
All datasets are deposited in zenodo.	This paper	https://doi.org/10.5281/zenodo.7014598
Experimental models: Cell lines		
hiPSC cell line	M. Hohwieler, et al., Human pluripotent stem cell-derived acinar/ductal organoids generate human pancreas upon orthotopic transplantation and allow disease modeling. Gut 66, 473–486 (2017).[26]	N/A
SOX2-T2A-tdTomato reporter hiPSC line	A. Shahryari, et al., Increasing Gene Editing Efficiency for CRISPR-Cas9 by Small RNAs in Pluripotent Stem Cells. CRISPR J 4, 491–501 (2021).[27]	N/A
Software and algorithms		
All source code files used within this paper are published on Github	This paper	1) https://github.com/marrlab/Bright2Nuc 2) https://zenodo.org/badge/latestdoi/519176662
Stardist	Weigert, M., et al. Star-convex Polyhedra for 3D Object Detection and Segmentation in Microscopy. 2020 Ieee Winter Conf Appl Comput Vis Wacv *00*, 3655–3662. 10.1109/wacv45572.2020.9093435.[15]	https://github.com/stardist/stardist
TrackMate	Tinevez, et al. (2016) TrackMate: An open and extensible platform for single-particle tracking. Methods San Diego Calif *115*, 80–90. 10.1016/j.ymeth.2016.09.016.[22]	https://imagej.net/plugins/trackmate/

RESOURCE AVAILABILITY

Lead contact

Further information and requests for resources and reagents should be directed to and will be fulfilled by the lead contact, Matthias Meier (matthias.meier@helmholtz-munich.de).

Materials availability

This study did not generate new unique reagents nor use new biological samples.

Data and code availability

Image data have been deposited at Zenodo and are publicly available as of the date of publication. DOIs are listed in the key resources table. All original code has been deposited at Github and is publicly available as of the date of publication. DOIs are listed in the key resources table. Bright2Nuc is available as a pip-installable package, together with commented analysis scripts at https://github.com/marrlab/Bright2Nuc. The dataset is made available via Zenodo with the https://doi.org/10.5281/zenodo.7014598. Any additional information required to reanalyze the data reported in this paper is available from the lead contact upon request.

EXPERIMENTAL MODEL AND STUDY PARTICIPANT DETAILS

When not specified otherwise, experiments were conducted using a hiPSC cell line[26] which was kindly provided by Prof. A. Kleger from Internal Medicine I, University Hospital, Ulm, Germany. The cell line was derived from a male patient. In some experiments for the acquisition of live fluorescence nuclear signals, a SOX2-T2A-tdTomato reporter hiPSC line was used, generated by Shahryari et al.[27] from Prof. H. Lickert Helmholtz Zentrum Munich. The cell line was derived from a female patient. Usage of the hiPSC was approved by the ethic commission of the Medical Faculty of TUM (reference number 400/21 S-KH). All cell lines were maintained in a pluripotent state as 2D adherent monolayers in conventional cell culture plates coated with Geltrex (Life Technologies, Cat#A1413302), fed daily using mTeSR Plus maintenance medium and maintained in a humidified atmosphere at 37°C and 5% CO_2. After reaching 70–80% confluence, the cells were passaged with 0.5 mM EDTA (AppliChem, Cat#A4892) in PBS. To enhance cell viability after splitting, the maintenance medium was supplemented with 10 μM ROCK inhibitor for the following 24 h. Mycoplasma-free cell culture was regularly confirmed using a MycoAlert Plus Mycoplasma Detection Kit (Lonza, Cat#LT07-703).

METHOD DETAILS

Microfluidic chip fabrication

PDMS chips were produced using traditional soft lithography techniques for two-layered devices.[13] Briefly, two molds were fabricated by photolithography. The mold for the control channel network was made to have features 25μm in height using SU-8 3025 (MicroChem, Cat #C1.02.003–0003). The mold for the flow flayer was fabricated in three steps. First, the flow channel was made using the AZ40XT photoresist (MicroChemicals, #104XT01) at a height of 40μm and re-flowed to obtain rounded half-channels. Second, the perfusion channels of the cell culture chambers were produced at a height of 20μm using SU-8 3025. Finally, the cell chambers were made using SU-8 3050 MicroChemicals, Cat# C1.02.003–0005) at a height of 50μm. All masks for photolithography were designed using the AutoCAD software (AutoDesk, 2019) and photoresists were patterned using a laser Micro Pattern Generator (μPG101, Heidelberg Instruments). All molds were coated with CYTOP (AGC Chemicals, Cat# CTL-809M) to prevent the adhesion of the PDMS. Chips were cast from the molds using Sylgard 184 PDMS (Dow Corning, Cat#DBE-712). The chips were assembled in a push-down configuration with the flow layer on the bottom. Flow and control layers were bonded using the off-ratio PDMS bonding procedure (5:1 pre-polymer to cross-linking reagents ratio for the control layer and 20:1 ratio for the flow layer). Finally, the flow layer was bonded to a glass slide carrier (Brain Laboratories, Cat#4450) through oxygen plasma activation (20 W at 0.9 mbar for 25 s). Each cell culture chamber comprised a central flow channel and two side channels bifurcating at the entry of the culture chamber. Pneumatic membrane valves divided the central flow channel into four 640 × 400μm^2 cell culture compartments with a volume of 0.013 μL. Gaps with a cross-section of 20 × 20μm^2 allowed the crossing of fluids between the side channels and the culture compartments.

Microfluidic chip operations

Pneumatic microfluidic valves (PMVs) within the chips were operated by applying a 1.5 mbar pressure on the control lines. The pressure could be switched on and off automatically on each control line using a homemade system enabling the individual control of 24 solenoid valves (SMC, Cat#LMV155RHY-5A-Q). Additionally, the system included a pressure regulator (Festo, Cat#VPPM-6L) connected to 8 additional solenoid valves which applied a controllable pressure (0–1.5 bar) on light-proof gas-tight bottles containing the reagents to be introduced in the chip. All connections were made using Tygon tubings (Proliquid, Cat# ND 100-80). Chips were placed in a microscope stage top incubator (Tokai Hit, Cat#STX) for maintaining a 37°C and 5% CO_2 humidified environment while allowing live imaging. Before cell seeding, the cell culture chambers were coated with a 10% Pluronic F-127 (Sigma-Aldrich, Cat#9003-11-6) in phosphate-buffered saline overnight to prevent cell adhesion to the glass substrate or PDMS walls. Adherent cells were harvested at 70–80%

confluence with TrypLE Express (Gibco, Cat# 12604013) and resuspended in 40–60 μL at a 1.5–3.5 × 10^8 cells/mL in maintenance medium (mTeSR Plus; StemCell Technologies, Cat#) supplemented with 10μM ROCK inhibitor (Y-27632, Santa Cruz Biotechnology, Cat#sc-281642A). For the formation of 3D cell cultures, a homogeneous single-cell solution was introduced into each cell culture chamber with PMVs in the open state. Upon actuation of the PMVs in the cell culture chamber, cells in the four compartments were isolated from the main flow stream, and cells in the side channels could be rinsed. Once seeded, cells were left to self-aggregate for 4 h before the first media renewal; media was then renewed in the cell culture chambers every 2 h using a 100 mbar forward fluidic pressure. The average diameter of on-chip 3D cell cultures depended on the single-cell solution density, i.e., 138 ± 13 μm for a cell density of 1.5 × 10^8 cells/mL and 243 ± 19μm for a cell density of 3.5 × 10^8 cells/mL. The 3D cell culture formation process after seeding was robust, as demonstrated by a low average coefficient of variation CV = 0.10 ± 0.05 and a chip-to-chip variation as low as CV = 0.08 (SI Figure S1).

Definitive endoderm differentiation

Before DE induction, cells were fed for 24 h with maintenance medium and ROCK inhibitor and another 24 h with maintenance medium only. DE differentiation was induced 48 h after on-chip seeding, the start of differentiation has been called 0 h in this paper. We followed the differentiation protocol as published in previous literature,[28] where the basal medium was supplemented with 100 ng/mL activin A (AA) (Peprotech, Cat# 120-14-300) and 3 μM CHIR-99021 (Tebu-bio, Cat#24804-0004) on the first day of differentiation. Basal medium supplemented with 100 ng/mL AA and 0.3 μM CHIR was added on the second day, and basal medium with 100 ng/mL AA was added on the third day of differentiation.

Immunocytochemistry on-chip

Partial fixations of 3D cell cultures (fixation of a subset of cell cultures in a single microfluidic platform, while keeping other cell cultures alive) were performed using NHS Ester (Bis-PEG4-NHS ester, BroadPharma, CAT#BP-21602). At the end of all experiments, before immunocytochemistry, all cell cultures were fixed in 4% paraformaldehyde in deionized water for 1 h (even if previously partially fixed NHS ester). Cell membranes were permeabilized with 0.2% Triton X-100 and 100 mM glycine in deionized water for 6 h and blocked in a blocking solution containing 3% donkey serum, 10% fetal calf serum, 0.1% Tween 20, and 0.1% bovine serum albumin (BSA) in PBS. Primary antibodies were diluted in the blocking solution and incubated in the cell culture chambers for 24 h before being rinsed away with PBS. Secondary antibodies and DAPI were then diluted also in the blocking solution and incubated for 24 h. All cell culture chambers were thoroughly rinsed with PBS prior to imaging. All steps were conducted on-chip and at room temperature. The antibodies used are listed in the key resource table.

Image acquisition

IF images and live bright-field images were acquired using a laser scanning confocal inverted microscope (Zeiss LSM 880 Airyscan) controlled by the ZEN Black version number software with a 20x/0.8-NA (numerical aperture) objective (Zeiss Plan-Apochromat 20x/0.8 M27), with up to five 8-bit or 16-bit data channels per image: transmitted light (bright-field using either the 633 nm or the 561 nm wavelength laser), DNA labeled with DAPI, and three types of antibodies distributed in the green (488 nm excitation), yellow (561 nm), and red (633 nm) channels. All images were acquired with a 0.25 × 0.25 $μm^2$ pixel size with the number of pixels being adjusted so that the scanning area could fit the imaged object in the frame (typical scanning areas were around 200 × 200 $μm^2$). Confocal stacks were acquired to image the full 50 μm z-depth of the 3D cell cultures with a z-resolution of 1 μm. For the imaging of fixed tissue, the pixel dwell time was kept in the 1–2 μs range, depending on scanning area size, with a 2-fold line averaging. For live tissue, pixel dwell times were reduced to the 0.6–0.9 μs range, to accelerate imaging so that a full confocal stack of a 3D cell culture could be acquired in less than 4 min.

Fluorescence signal correction

Prior to nuclear fluorescence signal quantification, two types of corrections were applied to the confocal image stacks. The first correction pertained to the weakening of fluorescence signals caused by the imaging depth in the 3D cell cultures. We calculated the relative average nuclear fluorescence signals (ratio between the average nuclear signal at a given depth and the average nuclear signal at the lowest point of the cell culture) as a function of the imaging depth. Under the assumption that nuclear signals should be constant on average relative to imaging depth, we calculated the imaging-depth decay rate through linear regression over all samples and for each wavelength. This wavelength-dependent correction was then applied to all image stacks. A second correction addressed antibody penetration inside the 3D cell culture during full-mount staining. Antibody penetration is a complex issue, which we resolved assuming that it factored in three main components: the antibodies, the x-y distance to the border of the cell culture, and the tissue type (differentiation state). We thus calculated the relative average nuclear fluorescence signal per antibody as a function of x-y distance to the border of the cell culture. The decay rates were calculated through linear regression per antibody for every sample within a time point to account for tissue type. All stacks were corrected under the assumption that nuclear signals should be constant on average relative to x-y penetration.

In silico nuclear staining

Bright2Nuc is a deep learning framework with a modified 3D U-Net,[29] based on the InstantDL[30] package, designed to predict nuclear markers from bright-field images (Figures 2A and 2B). Bright2Nuc works on 3D data, predicting the nuclear marker from slice to slice.

To incorporate 3D information from the bright-field image stack, we added nearest neighbor slices to the input of the network. Thus, three consecutive bright-field Z-slices (Z = k, Z = k-1, and Z = k+1 positions) are simultaneously considered by the model to predict each slice (Z = k) of the nucleus prediction. The U-Net architecture was modified from the 3D U-Net used in InstantDL by keeping the 3D convolutional layers the same but using anisotropic max-pooling in the encoder, and anisotropic up-sampling in the decoder, keeping the z-dimension unchanged. Bright2Nuc can be trained and evaluated using 3D stacks, through which it will automatically iterate during training, Bright2Nuc will crop or pad the input data to a size of 384 pixels in x-y dimension. During inference, it can handle arbitrary image sizes. If desired, it can rescale the images to keep the nuclei diameter constant, which simplifies transfer learning between datasets. An average nucleus diameter of 30 pixels worked best for our model. All considered images were bilinearly downscaled by a factor of 2 to a 0.5 μm/px xy-resolution before being processed for further analysis. We trained Bright2Nuc (i) on 162 fixed 3D cell culture images in 3D in bright-field and with a DAPI staining and (ii) on 93 cell cultures recorded in 3D in live tissue in bright-field and with a SOX2-T2A-tdTomato reporter signal. Together, we used approximately a quarter million nuclei/cells. For training, we optimized a mean squared error loss for 50 epochs with a batch size of 5. For data augmentation, we used brightness and contrast shifts of 30% of the pixel values, horizontal and vertical flips, and zooms with a maximum of 30% of the image size. The test set contained 85 cell cultures split in a stratified manner from the experimental data, summing up to around 80.000 cells/nuclei. Bright2Nuc is a ready-to-use python package, it can be downloaded via GitHub or installed using pip install and comes with our pre-trained model.

Nuclei segmentation

We trained two StarDist 3D models, one to segment cell nuclei from images of a nuclear marker staining (stardist_nuc), and one to segment 3D cell cultures with an *in silico* staining (stardist_silico). We manually segmented five 3D cell cultures and trained stardist_nuc on the corresponding DAPI staining. To train stardist_silico, we created a training set of 15 3D cell cultures. We used the same five manually segmented cell cultures with the corresponding DAPI staining adding the same five *in silico* stained cell cultures to the training set. Additionally, five *in silico* stained 3D cell cultures from the SOX2-T2A-tdTomato-reporter dataset were added, for which the segmentation *in silico* ground truth was obtained by segmenting the SOX2-T2A-tdTomato signal using the first Stardist model trained on DAPI and manually verifying the results, summing up to 15 cell cultures. We trained the models as described in the StarDist documentation, but changed the anisotropy to two (x: 0.5, y: 0.5, z: 1) to match our imaging resolution. To adapt the StarDist model to the live tissue data, we found it sufficient to lower the StarDist threshold to 0.29 without retraining the stardist_silico model (SI Figure S8). With two resulting models (one for DAPI, one for *in silico*) we segmented all DAPI stained 3D cell cultures and the *in silico* stained 3D cell cultures used in this paper.

Transcription factor expression prediction

To assess the differentiation status of single nuclei, we formulated the expression of the pluripotent marker OCT4 (e_{OCT4}), and the two differentiation markers FOXA2 (e_{FOXA2}) and SOX17 (e_{SOX17}) as a single ratio called differentiation label (DL) (SI Figure S4). Single-nuclei TFs expression were extracted from the corrected IF images (see fluorescence signal correction in materials) by calculating the average fluorescence over each of the 3D DAPI StarDist segmentations. TFs expressions were normalized per dataset between 0 and 1 to the 1-th and 99-th percentiles, respectively. DL was then calculated for each nucleus as:

$$DL = \frac{1}{1+\frac{2e_{OCT4}}{e_{FOXA2}+e_{SOX17}}}$$

From each segmented nucleus, 56 bright-field and 64 morphological features were extracted. The data were then randomly split into 5-folds, with an 80%/20% ratio between train and test set, and a random forest regressor was trained with 1000 estimators on each fold. In total, five random forest models were trained using the scikit-learn[31] framework in a round-robin fashion, splitting 20% of the nuclei into test sets iteratively so that each nucleus was contained in the test set once.

Live cell tracking

Single nuclei from the live *in silico* stained 3D cell cultures were tracked with TrackMate,[22] using the integrated LoG detector with a sigma of 22 pixels (11 μm) and a quality threshold of 10. Data anisotropy was accounted for by setting the x- and yvalues to 0.5 μm (leaving the z-value at 1 μm). The maximum linking distance was set to 22 pixels (11 μm) and the frame gap to two frames and 22 pixels. Tracking results were saved as a.csv file and evaluated in Python using pandas.[32] Predicted tracks outside the cell culture were filtered out using neighborhood-based filtering, removing all tracks that have less than 5 neighbors in a distance of 50 pixels per time point. Effective displacements were calculated as the effective distance over five frames divided by the time, with the effective distance being the distance between the centers of mass of the considered nucleus between the first and fifth frames. Directionality was also calculated over five frames as the ratio of the effective distance and the total distance, with the total distance being the sum of distances between the centers of mass and between all considered frames.

Single-cell analysis

For the single-cell analysis the raw data from the hiPSCs differentiation toward DE from Cuomo et al.[21] was downloaded and reprocessed. For quality filtering, cells with less than 1200 genes were excluded, as were genes present in a maximum of 2 cells. In addition, all cells expressing more than 15% mitochondrial genes were excluded. Expression was normalized to 10000 counts per cell. After determining the variable genes, total counts and the percentage of mitochondrial genes were regressed for further analysis. For the

calculation of neighbors, 24 PCs and 10 next neighbors were used according to the elbow method. The UMAP plot shown in SI Figure S10 was plotted with an initial position of the previously calculated PAGA graph. The Paga graph was computed using a Leiden clustering (data not shown) with a resolution 0.4.

QUANTIFICATION AND STATISTICAL ANALYSIS

Quantification and statistical analysis can be found in the text and figure legends. The statistical test, the number of samples n and the quantity measured is reported at the corresponding section in the text or figure legend.